Journal of Materials Research and Technology 42 (2026) 6928–6941

Contents lists available at ScienceDirect

Journal of Materials Research and Technology

journal homepage: www.elsevier.com/locate/jmrt

Influence of graphene reinforcement on the mechanical and tribological characteristics of AA2198T8–AA2024T3 friction stir welded joints

Ambuj Saxena [a], Vineet Singh [b], Shashi Prakash Dwivedi [c], K. Kumar [d,*], Wilson Kosasih [e,**], Najihah Mohd Tamyis [d], Ankit Sharma [f], Ashish Kumar [g]

[a] Department of Mechanical Engineering, G. L. Bajaj Institute of Technology and Management, Greater Noida, 201306, India
[b] Department of Mechanical Engineering, School of Engineering & Technology, IFTM University, Moradabad, 244102, India
[c] Department of Mechanical Engineering, Lloyd Institute of Engineering & Technology, Knowledge Park II, Greater Noida, Uttar Pradesh, 201306, India
[d] Universiti Kuala Lumpur, Malaysian Institute of Aviation Technology (UniKL MIAT), Lot 2891 Jalan Jenderam Hulu, 43800, Dengkil, Selangor, Malaysia
[e] Department of Industrial Engineering, Universitas Tarumanagara, Jakarta, 11440, Indonesia
[f] Centre for Research Impact & Outcome, Chitkara University Institute of Engineering and Technology, Chitkara University, Rajpura, 140401, Punjab, India
[g] Division of Research and Development, Lovely Professional University, Phagwara, India

ARTICLE INFO

Keywords:
Friction stir welding
AA2198–AA2024 dissimilar joints
Graphene nanoplatelets
Mechanical properties
Wear behavior
Dynamic mechanical analysis

ABSTRACT

This paper discusses the short-coming of decreased mechanical and tribological actions in dissimilar friction stir welded (FSW) joints of precautionary hardened aluminum alloys, especially AA2198-T8 and AA2024-T3, due to thermal softening and microstructural instability in the stir zone. Its main objective is to examine the impact of graphene nanoplatelet reinforcement on mechanical, tribological, and dynamic mechanical behavior of similar and dissimilar FSW joints. In this study, controlled FSW parameters were used to produce similar (AA2198+AA2198, AA2024+AA2024), dissimilar (AA2198+AA2024) and graphene-reinforced dissimilar joints (0.3 wt%). Systematic characterization of joints was done by tensile testing, hardness mapping, pin-on-disc wear testing, and dynamic mechanical analysis (DMA), and SEM/EDS microstructural analysis. The results demonstrate that graphene reinforcement significantly enhances joint performance, with the dissimilar reinforced joint exhibiting a yield strength of ~398 MPa, ultimate tensile strength of ~505 MPa, and ~99% joint efficiency. Improved hardness (~149 HV), reduced specific wear rate (~4.83×10^{-4} $mm^3/N{\cdot}m$), and lower coefficient of friction (~0.34) were observed due to grain refinement, dislocation pinning, and effective load transfer. DMA results further revealed enhanced stiffness retention, higher damping viscosity, and improved thermal stability of the reinforced joint. Fractographic analysis confirmed predominantly ductile failure with refined microstructural features. Overall, the study establishes graphene reinforcement as an effective strategy to overcome weld-zone softening and enhance the multi-functional performance of dissimilar FSW joints for advanced structural applications.

1. Introduction

Advanced Al-Cu-Li and Al-Cu-Mg alloys, such as AA2198 and AA2024, are a part of the modern aerospace structures due to their high strength-to-weight ratio, fracture toughness, and fatigue resistance. The addition of lithium to AA2198 increases the elastic modulus and reduces the density, while AA2024 remains a standard for damage tolerable airframe components. Nevertheless, welding of these precipitation-hardened alloys by fusion routes usually leads to hot cracking, porosity and serious precipitate degradation. Alemdar et al. [1] and Khalilabad et al. [2] showed that friction stir welding (FSW) is a method which dramatically increases the structural integrity in comparison to fusion processes, but thermal instability in the stir zone (SZ) is still a critical factor. Subsequent investigations have questioned the mechanical response of dissimilar AA2198+AA2024 FSW joints. Khalilabad et al. [3] reported the significant effect of tool geometry and welding speed on tensile strength and nugget morphology, while Masoumi Khalilabad et al. [4] reported the effect of post weld heat treatment on microstructure recovery. Microstructural examinations of Robe et al. [5] and Texier et al. [6] showed equiaxed recrystallized grains and

---

* Corresponding author.
** Corresponding author.
E-mail addresses: kkumar080680@gmail.com (K. Kumar), wilsonk@ft.untar.ac.id (W. Kosasih).

https://doi.org/10.1016/j.jmrt.2026.04.208
Received 14 March 2026; Received in revised form 21 April 2026; Accepted 23 April 2026

mechanical heterogeneities throughout the dissimilar interface, which directly influences strain localization. Nayan et al. [7] confirmed degradation of T1 (Al_2CuLi) precipitates in AA2198 whereas Paliwal et al. [8] demonstrated that thermomechanical history plays a significant role in ageing response. In the AA2024 weld nuggets, Moghadam and Farhangdoost [9] found reduced fracture toughness and faster fatigue crack propagation. Complementary fracture mechanics analyses by Kashaev et al. [10] highlighted the tendency of Al-Cu-Li systems to suffer from thermal residual stresses. Environmental degradation impact on the further worsening of the joint performance Exfoliation corrosion and surface instability has been discussed by Alemdar et al. [11], Vourdas et al. [12] and de Sousa Araujo et al. [13]. Interfacial phase evolution in dissimilar sheets was comparatively examined by Jandaghi et al. [14] and lap configurations manifested analogous heterogeneity influences according to Astarita et al. [15]. More recently, defect mitigation strategies were proposed by Suresh et al. [16], where Samir et al. [17] summarises comprehensive mechanical - microstructural correlations. Critically, the available literature focuses primarily on quasi-static tensile behavior and comparative analysis of similar and dissimilar joints processed in the same way is scarce. Moreover, tribological performance of AA2198-AA2024 systems is insufficiently addressed in spite of the fact that thermally softened SZ regions have inferior wear resistance due to the loss of hardness and the instability of precipitates [9]. Importantly, there is no systematic study to combine static mechanical properties, wear performance and dynamic mechanical response in a unified framework for similar and graphene modified dissimilar joints. Graphene, with ultra-high modulus (~1 TPa) and good tensile strength and intrinsic solid lubrication, is a promising solution to solve the issue of SZ softening. It can improve the transfer of loads and favor the refinement of the grain and reduce the adhesive wear by the formation of tribo-films. However, the effect of graphene incorporation on the coupled mechanical, tribological and viscoelastic behaviour of dissimilar AA2198 - AA2024 FSW joints is still largely unexplored. Dynamic Mechanical Analysis (DMA): more detailed information about temperature dependent viscoelastic behaviour: the storage modulus (E') elastic stiffness and load bearing capacity and the loss modulus (E') internal friction and energy dissipation. Damping factor ($\tan \delta = E''/E'$) is used as a measure of structural damping efficiency. The complex modulus, E^*, combines the elastic and viscous contributions, and the resistance to cyclic deformation and thermal softening is defined by the dynamic viscosity (η), and stiffness-loss slope (S). Incorporation of DMA parameters allows a more complete understanding of the microstructural stability and reinforcement efficacy under cyclic loading, of great relevance to aerospace service conditions. Accordingly, the present study represents a critical evaluation and comparison of the mechanical, tribological and the dynamic mechanical behavior of AA2198 base metal, AA2024 base metal, similar AA2198+AA2198 FSW joints, similar AA2024+AA2024 FSW joints, dissimilar AA2198+AA2024 FSW joints, and graphene reinforced dissimilar AA2198+AA2024 FSW joints containing 0.3 wt% graphene. By combining the tensile performance, wear properties and the DMA parameters (E', E'', $\tan \delta$, E, η, and S), the study in this work intends to construct a comprehensive relationship between structure and its mechanical properties, as well as to fill the current research gap on multi scale mechanical and tribological improvement of Al-Cu-Li/Al-Cu-Mg dissimilar welds. Recent studies have emphasized the importance of sustainable material design, advanced reinforcement strategies, and performance optimization of metallic systems for structural applications. For instance, Rehman et al. [18] highlighted the role of advanced material processing routes in improving recyclability and performance of engineering materials, while Kumar et al. [19] demonstrated the significance of microstructural tailoring in enhancing mechanical behavior under complex loading conditions. Similarly, recycling-based approaches and reinforcement strategies for improving tribological and mechanical performance have been reported in recent works [20], where the integration of secondary phases significantly improved wear resistance and structural stability. Investigations by Elsheikh et al. [21] and Hassan et al. [22] further confirmed that the incorporation of nano- and micro-scale reinforcements can effectively enhance strength, hardness, and durability of metallic systems through grain refinement and load transfer mechanisms. Further, application of nanoparticles in manufacturing process provides lighter, and more durable materials, resulting into innovations in aerospace, electronics, and biomedical engineering [23–25]. The nanomaterials have emerged as transforming force in manufacturing which delivers notable improvement in efficiency, sustainability, and precision [26]. However, despite these advancements, the available literature primarily focuses on either base materials or conventional composites, with limited emphasis on dissimilar friction stir welded Al–Cu–Li and Al–Cu–Mg systems, particularly under combined mechanical, tribological, and dynamic loading conditions. Moreover, the synergistic effect of graphene reinforcement on multi-scale performance (mechanical, wear, and viscoelastic behavior) of such dissimilar welded joints remains largely unexplored. Therefore, the present study aims to address this critical research gap by providing a comprehensive evaluation of graphene-reinforced AA2198–AA2024 dissimilar FSW joints, establishing a direct correlation between microstructure and multi-functional performance. The primary objective of this study is to systematically investigate the influence of graphene nanoplatelet reinforcement on the mechanical, tribological, and dynamic mechanical behavior of friction stir welded AA2198–T8 and AA2024–T3 aluminum alloys. Specifically, the study aims to: (i) compare the performance of similar and dissimilar FSW joints, (ii) evaluate the effectiveness of 0.3 wt % graphene addition in enhancing strength, hardness, and wear resistance, (iii) analyze the temperature-dependent viscoelastic behavior using dynamic mechanical analysis (DMA), and (iv) establish a comprehensive structure–property relationship by correlating microstructural evolution with mechanical and tribological responses. This integrated approach is intended to address the limitations of weld-zone softening and provide insights for improving the performance of dissimilar aluminum joints in advanced engineering applications.

2. Material and methods

2.1. Base material plates

The specimens utilized for the present research were AA2198-T8 and AA2024-T3 aluminium alloy plates, which were selected as representative base materials for the evaluation of the dissimilar welding performance in aerospace applications. AA2198-T8 is a third generation Al-Li alloy, known for its high specific strength and low density, which is mostly reinforced by T_1 (Al_2CuLi) and θ' (Al_2Cu) precipitates formed during solution treatment, cold forming and artificial ageing [1]. In contrast, AA2024 - T3 is a precipitation - hardened Al - Cu - Mg alloy whose mechanical properties are dominated by the Al2CuMg (S - phase) precipitates formed during solution treatment, cold working and natural ageing [3]. The differences in composition and precipitation behavior between these alloys significantly influence heat generation, material flow, and microstructural evolution during FSW. The nominal mechanical properties and chemical compositions are listed in Tables 1 and 2.

Table 1
Mechanical properties of base materials.

Property	AA2198-T8	AA2024-T3
Ultimate Tensile Strength (MPa)	542	525
Yield Strength (MPa)	400	325
Elongation (%)	14	18
Young's Modulus (GPa)	73	72
Hardness (HV)	160	140

Table 2
Chemical composition of welding plates (wt.%).

Element	AA2198-T8 (%)	AA2024-T3 (%)
Al	Balance	Balance
Cu	3.5	4.4
Li	1	—
Mg	0.5	1.5
Mn	0.35	0.6
Zn	0.3	0.25
Fe	0.3	0.5
Si	0.25	0.5
Ti	0.1	0.15

2.2. Reinforcement material

Graphene nanoplatelets (GNPs) were used as reinforcement in the dissimilar friction stir welded joints. The FSW was performed with a low level of 0.3 wt% graphene to the weld area to improve the mechanical and tribological properties of the joints. The reinforcement content which is selected is on the basis of previous research [27,28] which shows that low graphene additions will provide a uniform dispersion and less agglomeration thus increasing the strength enhancement efficiency. Graphene is a two-dimensional carbon nanomaterial with exceptional mechanical properties, including a Young's modulus of ~1 TPa and tensile strength of ~130 GPa, along with high thermal conductivity and excellent solid-lubrication characteristics [27,28]. When incorporated into aluminum alloys, graphene promotes grain refinement, load transfer strengthening, and dislocation pinning, which contribute to improved hardness and strength. Furthermore, graphene can form a protective tribological film at the contact interface during sliding, thereby reducing friction and wear. The chemical composition of the graphene nanoplatelets used in this study is presented in Table 3.

2.3. Friction stir welding process

Similar and dissimilar friction stir welding (FSW) was performed on AA2198-T8 and AA2024-T3 aluminum alloy plates with dimensions of 145 mm × 35 mm × 10 mm. Prior to welding, the plate surfaces were mechanically cleaned and rigidly clamped on a backing plate to prevent movement during the welding process. A non-consumable H13 tool steel tool with a cylindrical pin geometry (pin length: 3.6 mm, pin diameter: 4.67 mm) and a shoulder diameter of 18 mm was used to generate sufficient frictional heat and promote effective material plasticization and mixing. Welding was conducted at a tool rotational speed of 800 rpm, traverse speed of 200 mm/min, axial force of 10 kN, and a tool tilt angle of 2–3°. To facilitate effective material flow and mixing, AA2198-T8 was positioned on the advancing side and AA2024-T3 on the retreating side. The welding parameters used in this study were selected based on preliminary trials and established literature to ensure defect-free joints and stable material flow. All samples were processed under identical FSW conditions to isolate the influence of graphene reinforcement on the mechanical, tribological, and dynamic properties. While welding parameters significantly affect microstructural evolution and joint performance, the present work focuses on a comparative assessment under fixed processing conditions to clearly distinguish the effect of graphene addition. The welded region typically consisted of the stir zone (SZ), thermo-mechanically affected zone (TMAZ), and heat-affected zone (HAZ), representing the characteristic microstructural features of FSW joints. The schematic representation and experimental setup of the FSW process are illustrated in Fig. 1 (a) and 1 (b) respectively. Further, the FSW plate was mentioned in Fig. 1 (c). The combinations of similar and dissimilar joints prepared in this study are summarized in Table 4. In order to introduce the reinforcement into the weld region, a 2 mm deep and narrow longitudinal groove was machined along the joint interface of the plates prior to welding. The groove was filled with 0.3 wt% graphene nanoplatelets (GNPs) to facilitate their incorporation into the stir zone during the friction stir welding process.

Table 3
Chemical composition of graphene nanoplatelets.

Component	C	O	Si	Fe
Weight Percentage (wt.%)	98.8	0.7	0.3	0.2

During tool rotation and traversal, the severe plastic deformation and intense material flow generated by the rotating tool promoted the uniform dispersion of graphene within the weld nugget, leading to improved interfacial bonding and enhanced mechanical and tribological performance of the welded joint.

2.4. Tensile testing

The mechanical performance of the friction stir welded joints was evaluated through uniaxial tensile testing in accordance with ASTM E8/E8M standards. The experiments were conducted at room temperature using a computerized universal testing machine (UTM) at a constant strain rate of $1 \times 10^{-3}\ \mathrm{s}^{-1}$. Tensile specimens were extracted from the weld region using electrical discharge machining (EDM) with a gauge length of 20 mm to ensure dimensional accuracy and to minimize residual stresses during specimen preparation. The extraction location, and specimen geometry are illustrated in Fig. 1(c) and (d). The recorded load–extension data were converted into engineering stress–strain curves, from which the yield strength (YS), ultimate tensile strength (UTS), and elongation were determined. Engineering stress and engineering strain were calculated using Equations (1) and (2):

$$\sigma_{eng} = \frac{F}{A} \tag{1}$$

$$\varepsilon_{eng} = \frac{\Delta L}{L_0} \tag{2}$$

where σ_{eng} is the engineering stress (MPa), ε_{eng} is the engineering strain, F is the applied load (N), A is the original cross-sectional area of the gauge section (mm^2), ΔL is the change in gauge length (mm), and L_0 is the initial gauge length (mm). To account for the reduction in cross-sectional area during plastic deformation, the engineering values were converted into true stress–true strain using Equations (3) and (4):

$$\sigma_{true} = \sigma_{eng}\left(1 + \varepsilon_{eng}\right) \tag{3}$$

$$\varepsilon_{true} = \ln\left(1 + \varepsilon_{eng}\right) \tag{4}$$

The true plastic strain was then determined by subtracting the elastic component from the total true strain as expressed in Equation (5):

$$\varepsilon_{plastic} = \varepsilon_{true} - \frac{\sigma_{true}}{E} \tag{5}$$

where E represents the Young's modulus (MPa).

Finally, the plastic region of the true stress–strain curve was fitted using the Hollomon power law shown in Equation (6) to determine the strain hardening parameters:

$$\sigma_{true} = K\varepsilon_{plastic}^{n} \tag{6}$$

where K denotes the strength coefficient and n represents the strain hardening exponent. The resulting engineering, true, and strain-hardening behavior of the investigated materials are presented in Fig. 2(a–g), while the extracted mechanical parameters are summarized in Table 5.

2.5. Hardness test

The microhardness distribution of the similar and dissimilar friction stir welded (FSW) joints was evaluated using a Wilson Vickers

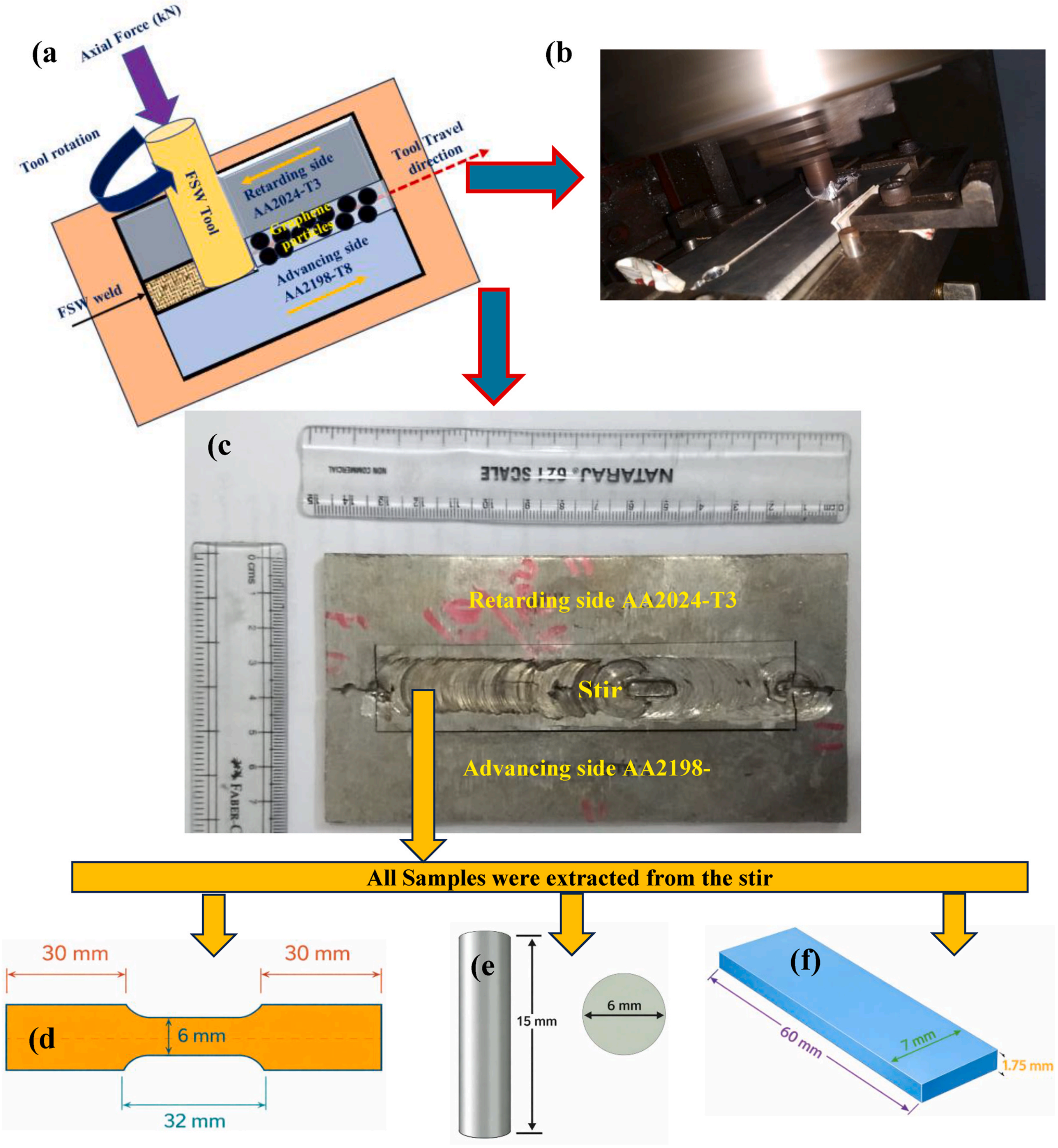

Fig. 1. (a) Schematic diagram of friction stir-welding, (b) Experimental friction stir welding, (c) Friction stir welded plate, (d) Schematic diagram of tensile test, (e) Schematic diagram of wear test, (f) Schematic diagram of DMA test.

Table 4
Developed similar and dissimilar FSW joint combinations.

Serial No.	Weld Plate-1	Weld Plate-2	Graphene Reinforcement (wt.%)
1	AA2198-T8	AA2198-T8	0
2	AA2024-T3	AA2024-T3	0
3	AA2198-T8	AA2024-T3	0
4	AA2198-T8	AA2024-T3	0.3

microhardness tester. Indentations were performed under a constant load of 0.5 kgf with a dwell time of 10 s to ensure consistent indentation and reliable measurements. The hardness measurements were taken along the transverse direction across the weld centerline to examine the variation in hardness within different weld regions, including the stir zone (SZ), thermo-mechanically affected zone (TMAZ), heat-affected zone (HAZ), and base material (BM). The obtained hardness profiles were used to analyze the influence of welding and graphene

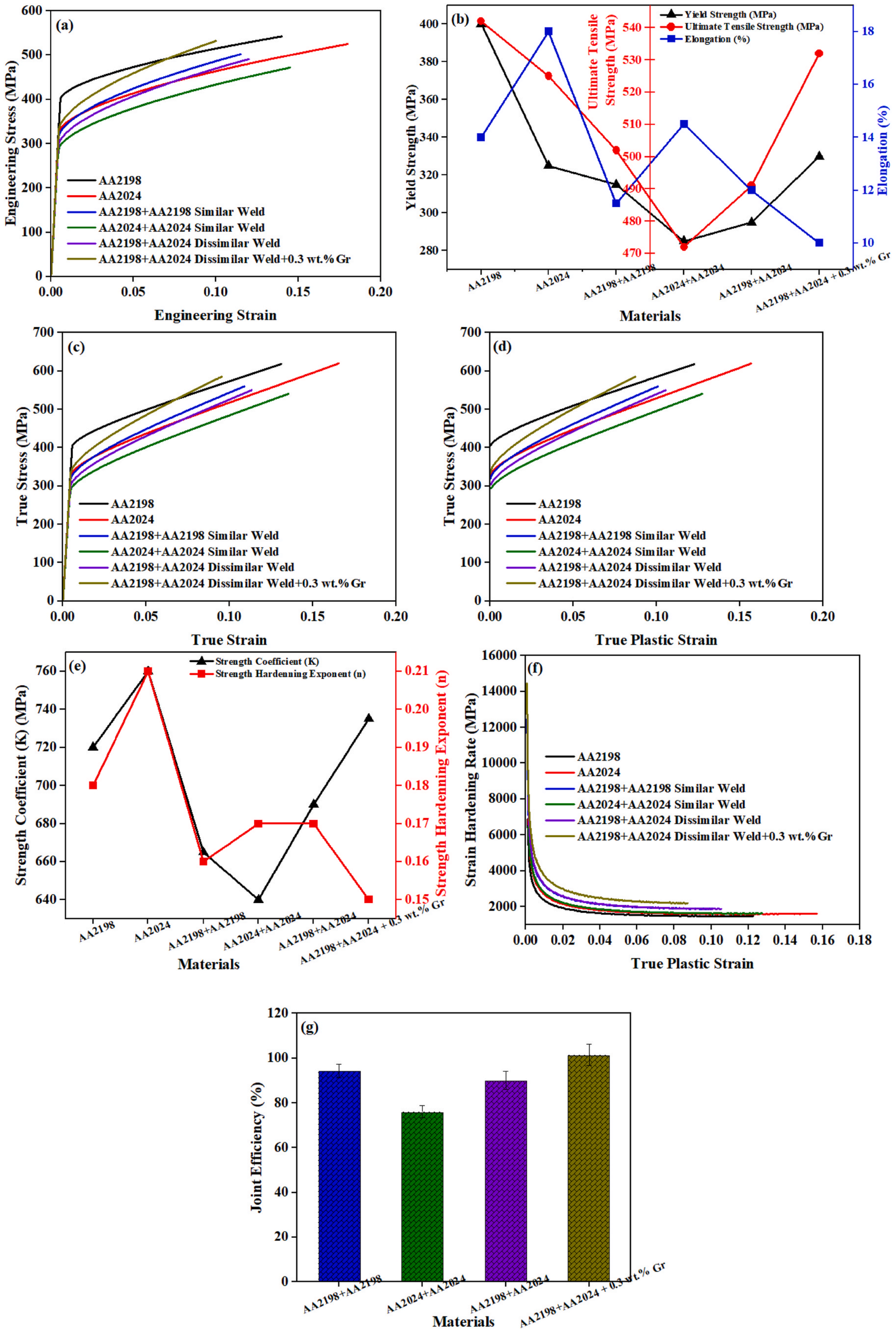

Fig. 2. (a) Engineering stress vs. engineering strain, (b) Yield, UTS and elongation for under investigated materials, (c) True stress vs. true strain curve, (d) True stress vs. true plastic strain curve, (e) K and n for under investigated material, (f) Strain hardening rate vs. True plastic strain, (g) Joint efficiency.

Table 5
Mechanical properties of material under investigation.

Material under investigation	Graphene (Wt.%)	Yield strength (MPa)	UTS (MPa)	K (MPa)	n	Elongation (%)	Joint efficiency (%)
AA2198-T8 Base Metal	–	455 ± 8	510 ± 10	845 ± 12	0.061 ± 0.003	11.5 ± 0.8	–
AA2024-T3 Base Metal	–	325 ± 7	470 ± 9	760 ± 11	0.089 ± 0.004	16.2 ± 1.1	–
AA2198-T8 Similar Weld	–	420 ± 9	480 ± 11	812 ± 13	0.068 ± 0.004	10.1 ± 1.2	94.12 ± 3.2
AA2024-T3 Similar Weld	–	305 ± 8	430 ± 10	735 ± 10	0.097 ± 0.004	14.5 ± 1.3	91.49 ± 2.9
AA2198-T8 + AA2024-T3 Dissimilar Weld	–	348 ± 10	455 ± 12	788 ± 11	0.082 ± 0.003	12.3 ± 1.4	89.22 ± 3.5
AA2198-T8 + AA2024-T3 Dissimilar Weld	0.3 wt%	398 ± 9	505 ± 13	835 ± 10	0.073 ± 0.003	13.6 ± 1.2	99.02 ± 4.1

reinforcement on the local mechanical behavior of the joints. The hardness profile os similar ad dissimilar FSW joins are mentioned in Fig. 3 (a).

2.6. Pin-on-disc wear testing

The wear behavior of the base materials and friction stir welded (FSW) joints was evaluated using a pin-on-disc tribometer under dry sliding conditions in accordance with ASTM G99 [29]. Wear specimens were extracted from the stir zone (SZ) to capture the tribological response of the modified weld microstructure. Cylindrical pin specimens of 6 mm diameter and 15 mm length (within the ASTM G99 standard pin diameter range of 2–10 mm) were prepared using electrical discharge machining (EDM) to isolate the stir zone and base material for comparative analysis [29]. This specimen geometry has also been widely adopted in tribological studies of aluminum alloys and FSW joints. Prior to testing, the specimen surfaces were polished and cleaned with ethanol.

Wear tests were conducted at normal loads of 30, 60, 90, and 120 N with a constant sliding distance of 2000 m, while the sliding speed was selected according to standard pin-on-disc testing practices reported in previous FSW wear investigations. The mass loss of each specimen was measured before and after testing using a precision electronic balance. The wear volume loss was determined using Equation (7):

$$V = \frac{\Delta m}{\rho} \tag{7}$$

where V is the volume loss (mm^3), Δm is the mass loss (kg), and ρ is the density of the material (kg/mm^3).

The specific wear rate was calculated using the Archard wear relationship given in Equation (8):

$$W = \frac{V}{F \times L} \tag{8}$$

where W is the specific wear rate (mm^3/N·m), F is the applied load (N), and L is the sliding distance (m).

The wear resistance was evaluated as the inverse of the specific wear rate according to Equation (9):

$$R = \frac{1}{W} \tag{9}$$

where R represents the wear resistance (N·m/mm^3).

The Archard wear coefficient was estimated using Equation (10):

$$k = \frac{V \times H}{F \times L} \tag{10}$$

where k is the dimensionless wear coefficient and H is the material hardness.

The coefficient of friction (COF) was continuously recorded during testing and calculated using Equation (11):

$$\mu = \frac{F_t}{F_n} \tag{11}$$

where μ is the coefficient of friction, F_t is the tangential friction force, and F_n is the applied normal load. The obtained mass loss, volume loss, specific wear rate, wear resistance, coefficient of friction, and Archard wear coefficient plots for all investigated materials are illustrated in Fig. 3(b–g).

2.7. Dynamic mechanical analysis (DMA)

Dynamic mechanical analysis (DMA) was used to determine the temperature-dependent viscoelastic properties of the base materials as well as the friction stir welded joints. Rectangular specimens were removed from the stir zone through wire-cut electrical discharge machining (EDM) to ensure fidelity of dimensions and to avoid thermal degradation. The dimensions of these specimens were 60 mm × 7 mm × 1.75 mm [30,31]. DMA testing was conducted under oscillatory loading under a three-point configuration, and the temperature increased from 30 °C to 380 °C with a constant rate of change under a constant rate of oscillation of 1 Hz. In the storage modulus (E'), loss modulus (E''), and damping factor (tan δ) were measured as a function of temperature. The storage modulus, representing the elastic energy stored in the material during cyclic deformation, was calculated using Equation (12):

$$E' = \frac{\sigma_0}{\varepsilon_0}\cos\delta \tag{12}$$

where σ_0 is the applied stress amplitude, ε_0 is the strain amplitude, and δ is the phase angle between stress and strain. The loss modulus, which represents the viscous energy dissipated during cyclic deformation, was determined using Equation (13):

$$E'' = \frac{\sigma_0}{\varepsilon_0}\sin\delta \tag{13}$$

The damping factor (tan δ), indicating the ratio of viscous to elastic response of the material, was calculated according to Equation (14):

$$\tan\delta = \frac{E''}{E'} \tag{14}$$

The dynamic viscosity (η) associated with the viscoelastic response was estimated using Equation (15):

$$\eta = \frac{E''}{\omega} \tag{15}$$

where $\omega = 2\pi f$ is the angular frequency and f is the oscillation frequency.

Furthermore, the stiffness-loss slope (S) was used to quantify the rate of stiffness degradation with temperature and was determined from the slope of the storage modulus–temperature curve as expressed in Equation (16):

$$S = \frac{dE'}{dT} \tag{16}$$

where T represents temperature. The variations of storage modulus, loss modulus, tan δ, dynamic viscosity, and stiffness-loss slope with temperature for all investigated materials are presented in Fig. 4(a–d).

3. Result and discussion

3.1. Plastic flow behavior of similar and dissimilar FSW joints

Fig. 2(a) shows the engineering stress–strain curves of the base

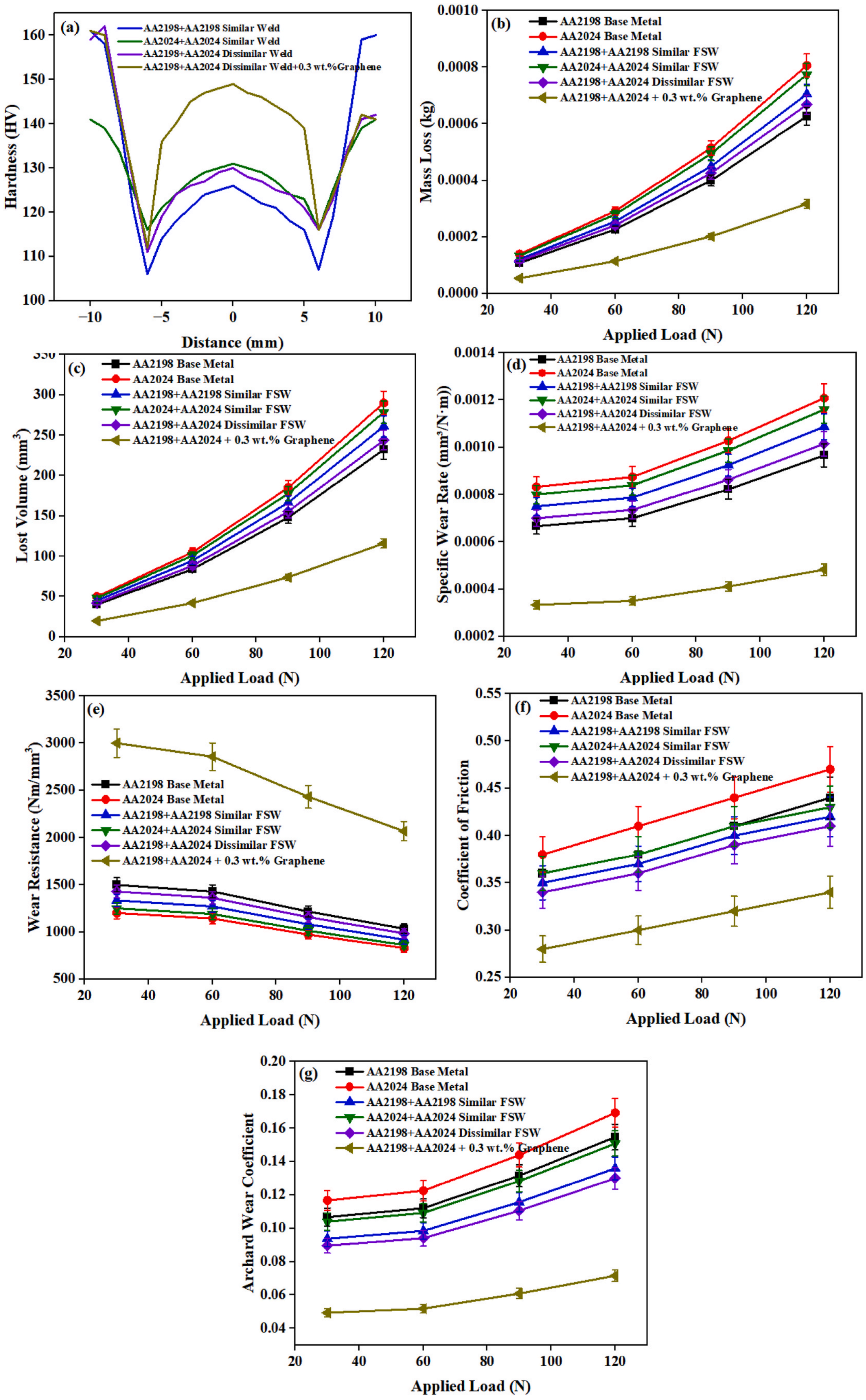

Fig. 3. Under investigation materials curves (a) Hardness profile, (b) Mass loss vs. load, (c) Lost volume vs. load (d) Specific wear rate vs. load (e) Wear resistance vs. load, (f) Coefficient of friction vs. load, (g) Archard Wear Coefficient vs applied Load.

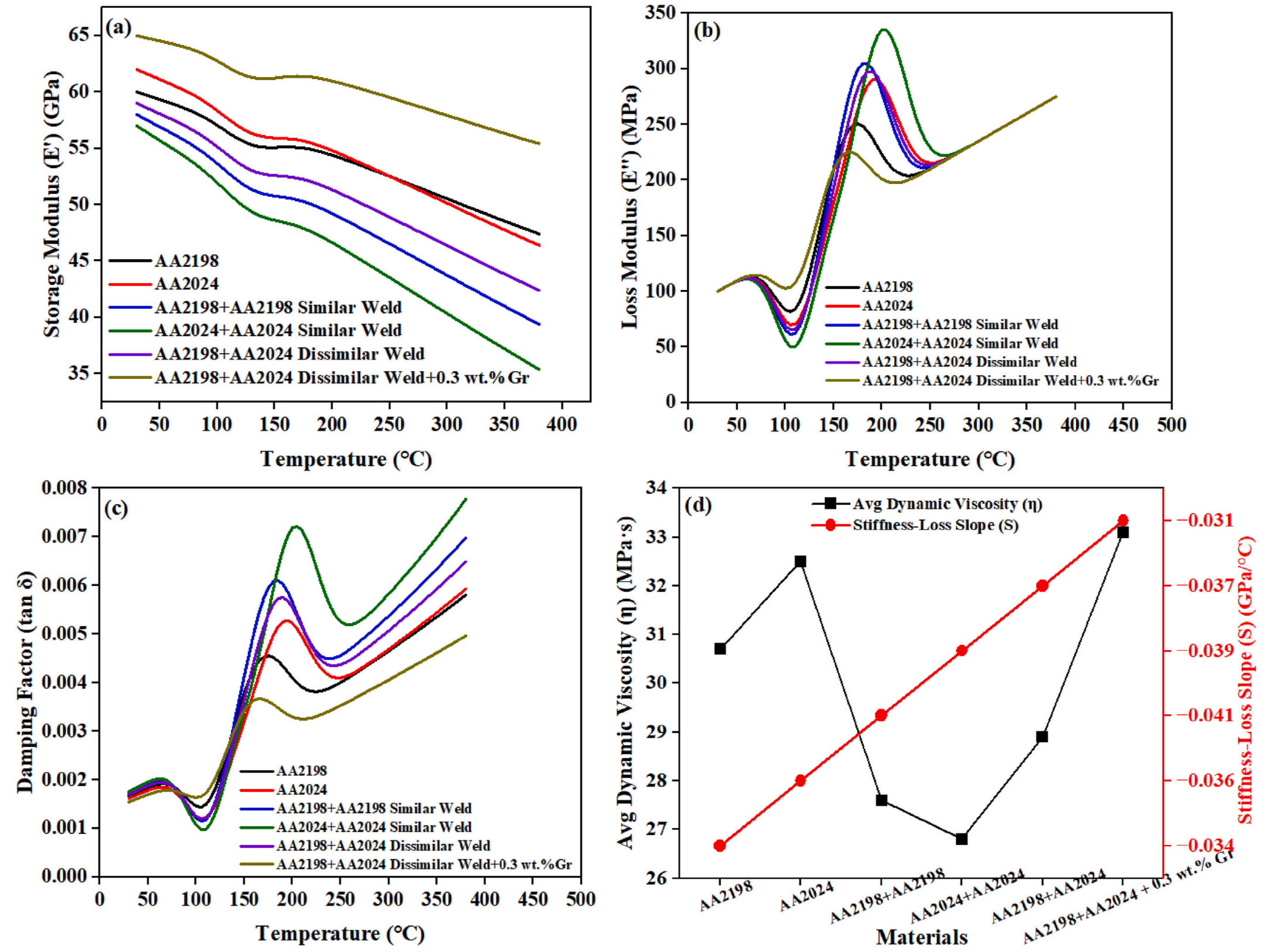

Fig. 4. Under investigation materials curves (a) Storage modulus vs. Temperature, (b) Loss modulus vs. Temperature, (c) Tan δ vs. Temperature, (d) Average damping viscosity and stiffness-loss slope.

materials and the corresponding FSW joints, while the summarized mechanical properties are presented in Table 5. The base alloys exhibit higher strength and ductility compared with the welded joints due to their uniform microstructure and absence of welding-induced thermal effects. AA2198-T8 shows the highest strength with a yield strength of 455 MPa and ultimate tensile strength of 510 MPa, attributed to precipitation strengthening from T_1 (Al_2CuLi) phases. AA2024-T3 exhibits slightly lower strength (YS ≈ 325 MPa, UTS ≈ 470 MPa) but relatively higher ductility due to the Al–Cu–Mg precipitation system. The FSW joints exhibit comparatively lower strength due to thermal softening, precipitate dissolution, and microstructural heterogeneity in the stir zone (SZ), thermo-mechanically affected zone (TMAZ), and heat-affected zone (HAZ). The AA2198–AA2198 similar weld shows a yield strength of about 420 MPa and UTS of 480 MPa, while the AA2024–AA2024 joint exhibits lower strength (YS ≈ 305 MPa, UTS ≈ 430 MPa). The AA2198–AA2024 dissimilar weld demonstrates intermediate mechanical properties (YS ≈ 348 MPa, UTS ≈ 455 MPa) due to asymmetric material flow and heterogeneous microstructural evolution across the weld interface.

The addition of 0.3 wt% graphene significantly improves the tensile strength of the dissimilar joint (YS ≈ 398 MPa, UTS ≈ 505 MPa) through grain refinement, dislocation pinning, and load-transfer strengthening, although the elongation slightly decreases due to restricted plastic deformation. The overall mechanical properties of all materials are summarized in Fig. 2(b) and Table 5. Fig. 2(c) presents the true stress–true strain curves, where the stress continuously increases with strain due to the progressive reduction in cross-sectional area during plastic deformation. The base alloys exhibit higher work-hardening behavior, with AA2024 reaching ~619 MPa and AA2198 ~617 MPa true stress.

In contrast, the welded joints show lower stress levels because of precipitate dissolution and microstructural softening within the welded regions. Among the welded conditions, the graphene-reinforced AA2198–AA2024 dissimilar joint shows the highest true stress (~585 MPa), indicating improved strengthening due to reinforcement-assisted load transfer. The true stress–true plastic strain curves shown in Fig. 2(d) further illustrate the strain-hardening behavior after yielding. The base alloys exhibit steeper hardening slopes due to efficient dislocation multiplication and uniform plastic deformation. However, the similar welded joints display reduced hardening capacity because of precipitate coarsening and softened microstructure in the weld region.

Comparative observations show that the graphene reinforced dissimilar weld has much better plastic flow resistance than the unreinforced variant. The parameters of the strain hardening objects from the Hollomon Equation (6) are tabulated in Fig. 2(e) and Table 5. Among the alloys, AA2024 is shown the highest strain-hardening exponent (ñ0.089) which is associated with a better work-hardening capability, while AA2198 has n ~ 0.061. The welded joint however shows lower values due to microstructural softening caused by welding. However, the strength coefficient (K) of the graphene-reinforced dissimilar joint is the largest (K ~ 835 MPa) for all welded conditions, which shows that the graphene-reinforced dissimilar joint has better resistance to plastic deformation. The variation of strain hardening rate (dσ/dε) with true plastic strain, shown in Fig. 2(f), reveals that all materials exhibit a rapid decrease in hardening rate during the initial stage of plastic deformation followed by a gradual stabilization at higher strain levels. This behavior corresponds to the transition from rapid dislocation multiplication to dynamic recovery mechanisms. In comparison to the other base alloys, AA2024 has a relatively higher and more stable strain hardening rate (~1600-1900 MPa) as compared to AA2198 (~1450-1500 MPa). Similar behavior is observed in the welded joint whose lower hardening rates are due to thermal softening and grain coarsening in the weld zone. Nevertheless, the graphene-reinforced dissimilar weld has relatively higher hardening rates (~2200 - 2400 MPa) compared to the other welded joints, which confirms the contribution of the strengthening of the graphene particles by the pinning of the dislocations and the increase in resistance to plastic deformation. Finally, Fig. 2(g) presents the joint efficiency of the welded conditions, calculated based on the tensile strength of the base alloys. The similar welds show efficiencies of approximately 94.12% (AA2198–AA2198) and 91.49% (AA2024–AA2024), while the dissimilar AA2198–AA2024 joint exhibits ~89.22% efficiency. The incorporation of 0.3 wt% graphene significantly improves the joint efficiency to approximately 99%, indicating that graphene reinforcement effectively compensates for welding-induced softening and enhances the load-bearing capacity of the dissimilar FSW joint. The results demonstrate that while friction stir welding reduces the strain-hardening capability relative to the base materials, graphene reinforcement significantly enhances the mechanical performance and joint efficiency of the dissimilar AA2198–AA2024 welded joint. Combined strengthening mechanisms, such as the refinement of grains, pinning of dislocations, and load transfer, can explain the improved mechanical performance of the graphene-strengthened dissimilar joint. The extreme plastic deformation under friction stir welding favors dynamic recrystallization leading to fine equiaxed grains in the stir zone which is very strong as per the Hall-Petch relation. Furthermore, graphene nanoplatelets are effective barriers to dislocation movement, enhance strengthening by Orowan-style processes and their homogeneous dispersion can result in efficient load transfer at the matrix reinforcement interface. Concrete evidence of the enhanced resistance to plastic deformation is also found in the greater strength coefficient (K) and the higher strain hardening rate, which is due to the limited dislocation mobility. Further, the high joint efficiency (~99%) indicates that the reinforcement of graphene is efficient in countering the softening that occurs with the welding by stabilizing the stir-zone microstructure. These processes are in combination with the noticed enhancement of mechanical performance.

3.2. Hardness and wear behavior of similar and dissimilar FSW joints

The hardness distribution and tribological performance of the investigated materials are presented in Fig. 3(a–g), demonstrating the relationship between microstructural strengthening and wear performance under varying applied loads. Fig. 3(a) shows the microhardness distribution across the weld centerline for the similar and dissimilar FSW joints. All joints exhibit the typical W-shaped hardness profile, where the minimum hardness occurs in the heat-affected zone (HAZ) due to precipitate coarsening and thermal softening, while the stir zone (SZ) exhibits relatively higher hardness as a result of dynamic recrystallization and grain refinement. The difference in properties through the weld regions is dictated by the different microstructural properties of stir zone (SZ), thermo-mechanical influenced zone (TMAZ), and heat-influenced zone (HAZ). The SZ is comparatively harder as it undergoes dynamic recrystallization and grain refinement, with uniform dispersion contributing to strengthening especially in the graphene-reinforced joint. Conversely, the TMAZ exhibits mid-hardness, because of partial plastic deformation and non-uniform microstructure. The HAZ is generally the softest due to the coarsening of the precipitates and softening of the material through heat without experiencing any appreciable deformation. These changes are further affected in dissimilar joints by the asymmetric material flow and different thermal response of both AA2198 and AA2024, resulting in heterogeneity in the localization along the weld interface. The increased hardness and stability of the SZ of the graphene-reinforced joint show that there is better microstructural integrity as compared to the surrounding area. The AA2024-AA2024 similar weld exhibits a central hardness (~131 HV) a bit higher than that of the AA2198-AA2198 joint (~126 HV) because the Al-Cu-Mg alloy system is more strongly precipitated hardened.

The AA2198–AA2024 dissimilar weld exhibits intermediate hardness (~130 HV) due to microstructural mixing across the weld interface. Notably, the AA2198–AA2024 + 0.3 wt% graphene joint exhibits the highest hardness (~149 HV), indicating reinforcement-assisted strengthening through grain refinement and dislocation pinning. The effect of hardness on wear behavior is seen in Fig. 3(b) which plots the mass loss against a load. For all materials, mass loss is increasing with load increase from 30 N to 120 N corresponding to intensified adhesive and abrasive wear under high contact stresses. The base alloy, AA2024, exhibits the highest mass loss, while the graphene-reinforced dissimilar weld exhibits the lowest mass loss in agreement with the higher hardness of the graphene-reinforced dissimilar weld shown in Fig. 3(a). Similarly, Fig. 3(c) shows the lost wear volume as a function of applied load, in which the wear volume gradually increases with load for all materials. The AA2024 base alloy exhibits the maximum lost volume (~290 mm^3 at 120 N), indicating greater material removal due to lower resistance to plastic deformation. On the other hand, the graphene reinforced dissimilar weld shows the least wear volume (~116 mm^3 at 120 N), indicating the positive influence of graphene reinforcement on the load bearing capacity and wear reduction. The particular wear rate variation with applied load is shown in Fig. 3(d). The specific wear rate is increased when the load increases for all materials due to increased frictional interaction and surface damage. Among all the series, AA2024 base alloy has the highest specific wear rate (~1.21×10^{-3} mm^3/N·m at 120 N), and the graphene reinforced dissimilar weld has the lowest (~4.83×10^{-4} mm^3/N·m), indicating the improvement in wear performance by improved hardness and reinforcement strengthening. The inverse relation between wear rate and durability is represented in Fig. 3 (e), which gives the wear resistance as a function of applied load. Wear resistance decreases with load as a result of accentuated material removal. Nevertheless, the graphene reinforced dissimilar weld still has the highest wear resistance of ~2068 Nm/mm^3 at 120 N and the lowest wear resistance is observed in the AA2024 base alloy, which is consistent with its higher wear rate and mass loss. The coefficient of friction (COF) variation with applied load, shown in Fig. 3(f), indicates that the COF increases slightly with load for all materials due to increased contact pressure and frictional heating at the sliding interface. The AA2024 base alloy has the highest COF (~0.47 at 120 N) while the lowest COF (~0.34) is observed for the graphene reinforced dissimilar weld. This reduction in friction has been attributed to the solid-lubrication effect of graphene and enhanced load transfer in the microstructure of the reinforced stir zone. Finally, Fig. 3(g) shows the Archard wear coefficient as a function of applied load, and further details of the wear mechanism. The Archard wear coefficient increases with applied load for all materials, indicating an increased tendency for material removal during sliding contact. The AA2024 base alloy has the highest Archard coefficient (~0.169 at 120 N), which confirms the poor wear resistance of the alloy. In contrast, the AA2198+AA2024 + 0.3 wt% graphene dissimilar weld shows the lowest Archard coefficient (~0.071), which reveals the best resistance to adhesive and abrasive wear. This reduction in wear coefficient is attributed to graphene-assisted load transfer, grain refinement, and reduced friction at the sliding interface. The aggregate findings in Fig. 3(a–g) indicate that there is a close association of hardness and tribological performance where the graphene-reinforced dissimilar FSW joint has better hardness (Fig. 3(a)), lower mass loss (Fig. 3(b)), lower wear volume (Fig. 3(c)), lower specific wear rate (Fig. 3(d)), higher wear resistance (Fig. 3(e)), and lower coefficient of friction coefficient (Fig. 3(f)). The results of the study prove that the reinforcement with graphene is effective in improving tribological characteristics of dissimilar AA2198-AA2024 friction stir welded joints.

3.3. Dynamic mechanical analysis (DMA) behavior similar and dissimilar FSW joints

Fig. 4(a–d) shows the temperature-dependent dynamic mechanical response of the studied materials. The findings indicate that the welding configuration, and graphene reinforcement have an effect on the viscoelastic stiffness of the aluminum alloys and damping behavior. Fig. 4(a) indicates the storage modulus (E') versus temperature. The storage modulus of all materials slowly decreases with temperature between 30 °C and 380 °C, which means that the elastic stiffness is decreasing under the effect of thermal softening and the high mobility of the atoms.

Storage modulus of AA2024 base alloy is slightly higher than that of AA2198, which may be explained by the fact that the Al-Cu-Mg alloy system has a higher precision hardening property. The welded joints are slightly less stiff as a result of friction stir welding induced microstructural modifications on the joints. Nevertheless, the AA2198-AA2024 dissimilar weld reinforced with 0.3 wt% graphene exhibits the highest value of storage modulus over the temperature regime, which implies a better load transfer and stiffness stability due to graphene reinforcement and optimized stir-zone structure. Fig. 4(b) shows the change in the loss modulus (E'') with temperature. Loss modulus rises gradually with temperature and peaks in the middle temperature range (around 160–180 °C), and then gradually plateaus at higher temperatures. This action indicates a higher level of internal friction and energy loss that goes with thermally activated dislocation movement and microstructural relaxation. The welded joints tend to exhibit increased loss modulus as compared to the base alloys implying increased internal friction owing to heterogeneous microstructures in the stir zone. The graphene-reinforced dissimilar weld has the highest loss modulus amongst all the materials suggesting it has a better load absorption capacity during dynamic loading. Fig. 4(c) shows the damping factor (tan δ) which is the ratio of the loss modulus to storage modulus. The values of tan δ grow linearly with temperature, showing an improvement in damping characteristics as the material shifts to a more viscoelastic response at higher temperatures. The similar and dissimilar FSW joints are more damped than the base materials, which indicates that the grain refinement and microstructural heterogeneity in the stir zone affects the damping. The AA2198-AA2024 dissimilar weld that is reinforced with 0.3 wt% graphene, however, exhibits relatively lower tan δ values at elevated temperatures, which implies a higher stiffness retention and less energy loss as a result of the reinforcing effect of graphene. A comparative evaluation of average damping viscosity (η) and stiffness-loss slope (S) is presented in Fig. 4(d). The findings reveal that the graphene-reinforced dissimilar weld has the greatest damping viscosity (~33.1) which means that the weld is more resistant to dynamic deformation. Conversely, the welds of similar items exhibit lower values of damping viscosity (~2628) since they are not as stable in microstructure. The values of slope stiffness-loss are negative in all the materials, which proves the fact that with rise in temperature, there is gradual loss of stiffness. It is remarkable that the graphene-reinforced dissimilar weld has the lowest value of the slope of stiffness-loss (−0.031), indicating the best thermal stability among the tested materials. The results presented in Fig. 4(a–d) indicate that graphene reinforcement significantly improves the dynamic mechanical stability of AA2198–AA2024 dissimilar friction stir welded joints by enhancing stiffness retention, energy dissipation capability, and thermal stability under oscillatory loading conditions. The improved dynamic mechanical behavior of the graphene-reinforced joint can also be theoretically attributed to enhanced interfacial bonding and restricted molecular mobility within the microstructure. The presence of graphene increases stiffness retention by limiting thermally activated dislocation motion and microstructural relaxation at elevated temperatures. The higher damping viscosity and lower stiffness-loss slope indicate improved resistance to cyclic deformation, which can be correlated to effective stress transfer and energy dissipation mechanisms at the matrix–reinforcement interface.

3.4. Microstructural investigation

Fig. 5(a and b) shows the microstructure of the friction-stir zone (FSZ) obtained by SEM and EDS elemental mapping of AA2198-T8/AA2024-T3 joint reinforced with 0.3 wt% of graphene. Fig. 5(a) shows the fine, dynamically recrystallized microstructure in the stir zone which is a direct result of severe plastic deformation and frictional heating during the FSW process. The uniform dispersion of graphene particles in the aluminium matrix can be seen in the micrograph, which indicates good material flow and fair particle dispersion without agglomeration and void formation. Fig. 5(b) shows the EDS elemental mapping showing the distribution of the main elements Al, Cu, Mg, Li, Mn, Fe and C. The aluminum map corresponds to the continuous matrix whereas Cu and Mg are homogeneously distributed, which is a manifestation of the alloying contributions of AA2198 and AA2024. Carbon map checks existence and distribution of graphene reinforcement in the stir zone. The relatively homogenous distribution of elements shows an efficient intermixing and metallurgical bond obtained during the friction stir welding process that led to a structurally stable and reinforced weld region. In precipitation-hardened alloys such as AA2198 and AA2024, the strengthening phases primarily consist of T_1 (Al_2CuLi), θ' (Al_2Cu), and S-phase (Al_2CuMg) precipitates. During friction stir welding, the thermal cycle and severe plastic deformation in the stir zone lead to partial dissolution and coarsening of these precipitates, resulting in localized softening. However, the introduction of graphene nanoplatelets influences this evolution by promoting grain refinement and restricting atomic diffusion, which can limit excessive precipitate coarsening. The refined microstructure and improved hardness observed in the graphene-reinforced joint suggest a more stable precipitate distribution compared to the unreinforced condition. Although quantitative characterization of precipitate size and distribution is beyond the scope of the present study, the observed mechanical and microstructural responses are consistent with modified precipitate behavior and enhanced microstructural stability in the stir zone. Fig. 6(a and b) presents the morphology of worn surface of the friction stir zone (FSZ) of AA2198-T8/AA2024-T3 reinforced with 0.3 wt% graphene in the case of sliding wear test results obtained by SEM. As observed in Fig. 6(a), the wear surface has a shallow-parallel-grooves due to the sliding direction, so it can be inferred that abrasive wear is the dominant wear mechanism. The occurrence of compact debris clusters and plastically deformed areas within the marked area is indicative of localised material removal because of repeated sliding contact. Compared with typical wear surfaces of aluminium alloy, the grooves are relatively shallow, which indicates better wear resistance due to graphene reinforcement and refined stir zone microstructure. The magnified micrograph in Fig. 6 (b) clearly shows fine wear debris, micro ploughing tracks and broken particles embedded in the matrix. These characteristics are characteristic of a combination of mild abrasive wear and low adhesive wear. The dispersed graphene particles act as solid lubricants to reduce frictional shear stress and inhibit severe plastic deformation and delamination. Consequently, the wear surface exhibits less crack propagation and less delamination pits, showing the improved tribological performance of the graphene-reinforced dissimilar FSW joint. Overall, the SEM observations demonstrate that the AA2198-AA2024 + 0.3 wt% graphene stir zone experiences predominantly mild abrasive wear with reduced adhesive damage, which correlates well with the lower mass loss, reduced

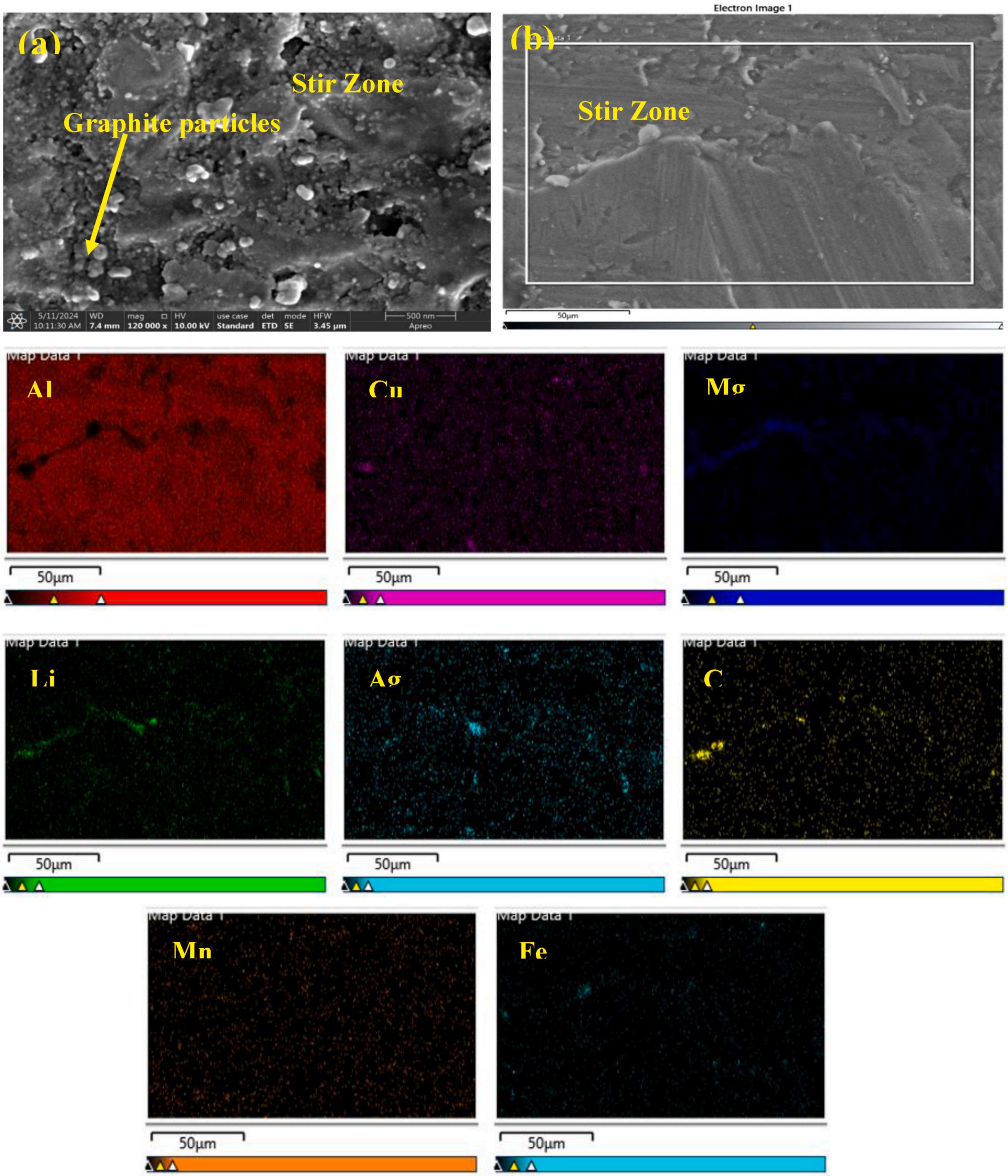

Fig. 5. (a) Scanning electron microscope micrograph of stir zone AA2198T8+AA2024T3 + 0.3 wt% Graphene, (b) EDS Mapping of stir zone AA2198T8+AA2024T3 + 0.3 wt% Graphene.

specific wear rate, and lower coefficient of friction reported in Fig. 3. Fig. 6(c) shows the SEM morphology of the tensile fracture surface of the friction-stir zone (FSZ) of the AA2198-T8/AA2024-T3 joint reinforced with 0.3 wt% graphene. The fracture surface is characterized by numerous ductile dimples and micro-void coalescence features, indicating that the failure predominantly occurred through a ductile fracture mechanism. The presence of tear ridges and plastically deformed ligaments between dimples suggests significant plastic deformation prior to final rupture. In addition, a few localized cleavage facets are observed, indicating minor brittle fracture contributions due

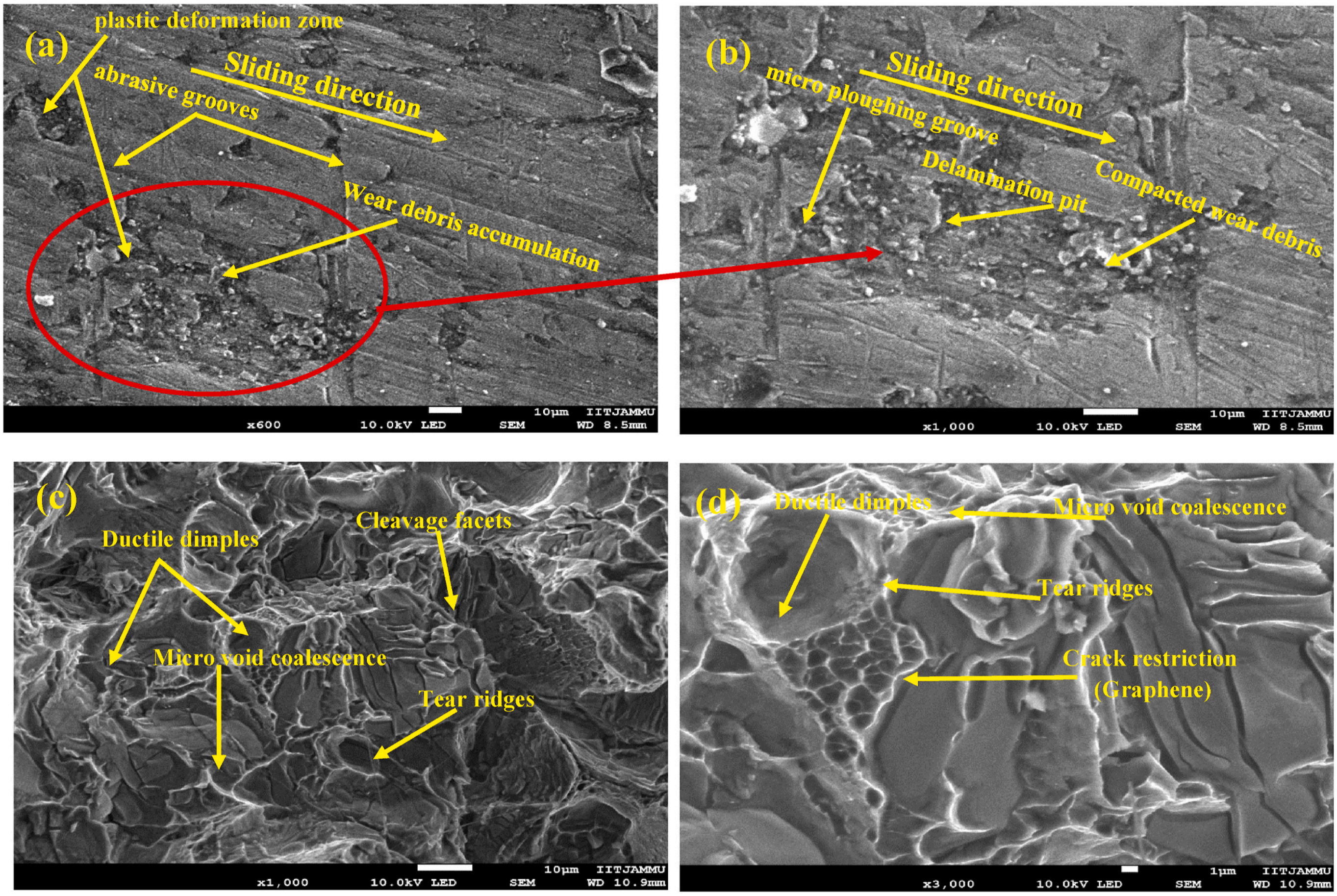

Fig. 6. Friction-stir zone AA2198–AA2024 + 0.3 wt% graphene: (a) wear SEM micrograph, (b) enlarged wear micrograph, (c) tensile fracture surface, (d) annotated fracture surface showing deformation and strengthening features.

to heterogeneous microstructural regions within the stir zone. The fine and well-spread dimples suggest efficient grain refinement and load transfer with the assistance of graphene particles, which postpones the crack formation and enhances the constant plastic deformation. Fine ductile dimples (indication of plastic deformation), micro-void coalescence (indication of dislocation-based fracture) and tear ridges (indication of strain localization) further prove increased deformation behavior as noted in Fig. 6(d). Besides, the recorded low crack propagation in the marked areas suggests the presence of graphene in hindering the dislocation motion and increasing the resistance to localized deformation. These characteristics are in line with the reinforcement-assisted strengthening mechanisms whereby graphene helps in enhancing the transfer of loads and microstructural stability in the stir zone. These fracture behavior findings support the high tensile ductility and strength of the graphene-reinforced dissimilar FSW joint that is in line with the high mechanical performance observed when tensile strength is considered. It is anticipated that the enhanced microstructural stability and homogeneous dispersal of graphene in the stir zone will impact positively on the service-related attributes, including fatigue property, fracture toughness, and corrosion characteristics. Its refined grain structure and increased load transfer has the ability to retard crack initiation and lower rates of crack propagation, which are vital to fatigue performance. Correspondingly, the ductile fracture features and limited crack propagation observed indicate enhanced fracture resistance. Moreover, the existence of graphene can help to decrease residual stresses and enhance corrosion resistance by restricting localized heterogeneity of microstructures and barrier diffusion. These effects suggest the possibility of the improved service performance of graphene-reinforced dissimilar joints.

4. Conclusions and scientific implications

4.1. Implications to theory and practice

The current research contributes to the basic knowledge of strengthening processes in the graphene-reinforced dissimilar friction stir welded (FSW) joints. Theoretically, the findings validate that the synergistic behavior of the grain refinement, dislocation pinning, and load transfer processes determines the strengthened mechanical and tribological behavior of the reinforced stir zone. The incorporation of dynamic mechanical analysis further extends the framework by linking microstructural stability with temperature-dependent viscoelastic behavior, thereby contributing to a more comprehensive structure–property relationship in welded aluminum systems. Practically, the results show that graphene nanoplatelet reinforcement is a viable approach to prevent weld-zone softening, and to substantially increase the joint efficiency, hardness, wear resistance, and thermal stability. These improvements are particularly relevant for aerospace and high-performance structural applications where dissimilar aluminum alloys are subjected to combined mechanical and tribological loading conditions.

4.2. Key lessons learned

The research points out that microstructural evolution in the stir zone is the main factor that governs the performance of dissimilar FSW joints. Introduction of a minor proportion of graphene (0.3 wt%) leads to significant gains in strength and wear resistance because of a successful dispersing the reinforcement and interaction with dislocations.

Moreover, the tensile, tribological and dynamic mechanical property are evaluated together, which gives a comprehensive insight into the material behavior under both the static and dynamic load conditions. The findings highlight the importance of reinforcement distribution, interfacial bonding, and process parameters in obtaining excellent joint performance.

4.3. Limitations and future scope

The current study has some limitations, despite the great findings. The study is limited to one level of reinforcement and a predetermined combination of process parameters, which can affect the applicability and extrapolation of the findings. Also, there was a lack of long term performance properties like fatigue life, corrosion resistance and environmental degradation. Further investigation of the optimization of reinforcement contents, hybrid or other forms of nano-reinforcements, and research on the structural integrity in the long term under service-relevant conditions should be considered as the future research to further confirm the applicability of graphene-reinforced dissimilar FSW joints.

4.4. Key findings and conclusions

Friction stir welding successfully produced defect-free similar and dissimilar joints of AA2198-T8 and AA2024-T3 alloys, with a refined stir-zone microstructure resulting from severe plastic deformation and dynamic recrystallization. The incorporation of 0.3 wt% graphene nanoplatelets significantly enhanced the mechanical performance of the dissimilar joint, leading to improved strength and a joint efficiency approaching 99%, primarily due to grain refinement, dislocation pinning, and effective load transfer mechanisms.

The graphene-reinforced stir zone exhibited superior hardness (~149 HV), which directly contributed to enhanced wear resistance. The improved tribological behavior, characterized by reduced material loss, lower specific wear rate ($\sim 4.83 \times 10^{-4}$ mm^3/N·m), and decreased coefficient of friction (~0.34), is attributed to the combined effects of increased hardness and the solid-lubricating nature of graphene, resulting in predominantly mild abrasive wear.

Furthermore, dynamic mechanical analysis confirmed improved viscoelastic stability of the reinforced joint, evidenced by higher stiffness retention, increased damping viscosity (~33.1), and a reduced stiffness-loss slope (-0.031), indicating enhanced resistance to thermal softening and cyclic deformation. The results establish that graphene reinforcement effectively improves the multi-functional performance of dissimilar FSW joints through microstructural stabilization and enhanced interfacial interactions.

Data availability statement

The data that support the findings of this study are available from the corresponding author upon reasonable request.

Funding statement

This research did not receive any specific grant from funding agencies in the public, commercial, or not-for-profit sectors.

Declaration of competing interest

The authors declare that they have no known competing financial interests or personal relationships that could have appeared to influence the work reported in this paper.

References

[1] Alemdar ASA, Jalal SR, Mulapeer MM. Effect of exfoliation corrosion on the efficient hybrid joint of AA2024-T3 and AA2198-T8 formed by friction stir welding. Helyon 2023;9(6).

[2] Khalilabad MM, Zedan Y, Texier D, Jahazi M, Bocher P. The influence of tool geometry on mechanical properties of friction stir welded AA-2024 and AA-2198 joints. In: 34th CONFERENCE AND EXHIBITION ICSOBA, vol. 34; 2016, October.

[3] Khalilabad MM, Zedan Y, Texier D, Jahazi M, Bocher P. Effect of tool geometry and welding speed on mechanical properties of dissimilar AA2198–AA2024 FSWed joint. Journal of Manufacturing Processes 2018;34:86–95.

[4] Masoumi Khalilabad M, Zedan Y, Texier D, Jahazi M, Bocher P. Effect of heat treatments on microstructural and mechanical characteristics of dissimilar friction stir welded 2198/2024 aluminum alloys. J Adhes Sci Technol 2022;36(3):221–39.

[5] Robe H, Zedan Y, Chen J, Monajati H, Feulvarch E, Bocher P. Microstructural and mechanical characterization of a dissimilar friction stir welded butt joint made of AA2024-T3 and AA2198-T3. Mater Charact 2015;110:242–51.

[6] Texier D, Zedan Y, Amoros T, Feulvarch E, Stinville JC, Bocher P. Near-surface mechanical heterogeneities in a dissimilar aluminum alloys friction stir welded joint. Mater Des 2016 Oct 15;108:217–29.

[7] Nayan N, Yadava M, Sarkar R, Murty SN, Gurao NP, Mahesh S, Prasad MJNV, Samajdar I. Microstructure and tensile response of friction stir welded Al–Cu–Li (AA2198-T8) alloy. Mater Charact 2020;159:110002.

[8] Paliwal, D., Trivedi, S., Yadava, M. and Nayan, N., Effect of pre-stretch on aging response of friction stir processed Al-Cu-Li (AA2198) alloy sheet. Available at: SSRN 6172460.

[9] Moghadam DG, Farhangdoost K. Influence of welding parameters on fracture toughness and fatigue crack growth rate in friction stir welded nugget of 2024-T351 aluminum alloy joints. Trans Nonferrous Met Soc China 2016;26(10): 2567–85.

[10] Kashaev N, Riekehr S, Erdmann K, Carvalho AA, Nurgaliev M, Alexopoulos N, Karanika A. Fracture mechanical behaviour of laser beam-welded AA2198 butt joints and integral structures. Int J Struct Integr 2015;6(6):787–98.

[11] Alemdar ASA, Jalal SR, Mulapeer MMS. Influence of friction stir welding process on the mechanical characteristics of the hybrid joints AA2198-T8 to AA2024-T3. Adv Mater Sci Eng 2022;2022(1):7055446.

[12] Vourdas N, Karanika A, Aldanondo E, Visser P, Van derGeest M. Effect of environmentally friendly surface treatments on the corrosion behavior of new al-cu-li alloys. Eng Fail Anal 2024;163:108487.

[13] de Sousa Araujo JV, Xavier Milagre M, Emil Klumpp R, Hugo Ayusso V, Donatus U, Costa I. TSA anodising voltage effects on the near-surface coarse intermetallic particles in the AA2024-T3 and AA2198-T8 alloys. Corrosion Eng Sci Technol 2022;57(4):380–96.

[14] Jandaghi MR, Pouraliakbar H, Saboori A, Hong SI, Pavese M. Comparative insight into the interfacial phase evolutions during solution treatment of dissimilar friction stir welded AA2198-AA7475 and AA2198-AA6013 aluminum sheets. Materials 2021;14(5):1290.

[15] Astarita A, Tucci F, Silvestri AT, Perrella M, Boccarusso L, Carlone P. Dissimilar friction stir lap welding of AA2198 and AA7075 sheets: forces, microstructure and mechanical properties. Int J Adv Manuf Technol 2021;117(3):1045–59.

[16] Suresh S, Natarajan E, Mohan DG, Ang CK, Sudhagar S. Depriving friction stir weld defects in dissimilar aluminum lap joints. Proc Inst Mech Eng Part E J Process Mech Eng 2026;240(1):433–44.

[17] Samir AA, Jalal SR, Mulapeer MM. Dissimilar joint welding through friction stir techniques: mechanical and microstructural properties of AA2198-T8 & AA2024-T3. 2023.

[18] Yusaf T, Mahamude ASF, Farhana K, et al. 20-A comprehensive review on graphene nanoparticles: preparation, properties, and applications. Sustain Times 2022;14. https://doi.org/10.3390/su141912336.

[19] Rehman A, et al. Sustainable material processing and recyclability enhancement in engineering systems. Results Chem 2023:101166. https://doi.org/10.1016/j.rechem.2023.101166.

[20] Kumar R, et al. Microstructural tailoring and mechanical performance optimization of advanced materials. Sci Rep 2024;14:62661. https://doi.org/10.1038/s41598-024-62661-4.

[21] Singh J, et al. Recycling strategies and reinforcement effects on mechanical and tribological performance of materials. Recycling 2023;8(5):65. https://doi.org/10.3390/recycling8050065.

[22] Elsheikh AH, et al. Enhancement of mechanical properties using nano-reinforcements in metallic systems. Egypt J Chem 2021;64(9). https://doi.org/10.21608/ejchem.2021.93980.4425.

[23] Singh P, Singh D, Patel A, Tripathi NM. Introduction to nanotechnology in manufacturing. In: Singh D, Tripathi NM, Sharma A, Saxena KK, Mishra RK, editors. Unraveling the potential of nanotechnology in next-gen manufacturing processes: a perspective of biomaterials. ASME Press; 2026. https://doi.org/10.1115/1.889411_ch1.

[24] Negi SS, Singh D, Dhiman VK, Dhiman VK, Verma SK, Nautiyal A. Nanotechnology in electronics: a game changer. In: Singh D, Tripathi NM, Sharma A, Saxena KK, Mishra RK, editors. Unraveling the potential of nanotechnology in next-gen manufacturing processes: a perspective of biomaterials. ASME Press; 2026. https://doi.org/10.1115/1.889411_ch6.

[25] Negi SS, Singh D, Khare R, Pandey A, Singh V, Pandey S. Role of biomaterials in nanotechnology. In: Singh D, Tripathi NM, Sharma A, Saxena KK, Mishra RK, editors. Unraveling the potential of nanotechnology in next-gen manufacturing processes: a perspective of biomaterials. ASME Press; 2026. https://doi.org/10.1115/1.889411_ch2.

[26] Eyube MO, Enuesueke C, Alimikhena M. The future of nanomaterials in manufacturing. In: Singh D, Tripathi NM, Sharma A, Saxena KK, Mishra RK, editors. Unraveling the potential of nanotechnology in next-gen manufacturing processes: a perspective of biomaterials. ASME Press; 2026. https://doi.org/10.1115/1.889411_ch18.

[27] Hassan M, et al. Effect of reinforcement particles on structural and mechanical behavior of advanced materials. Egypt J Chem 2021;64(8). https://doi.org/10.21608/ejchem.2021.89060.4276.

[28] Ojrzyńska M, Daniewski AR, Wilczyński K, et al. 21-High-Quality graphene nanoplatelets production with 100% yield based on popular fertilizer industry feedstock. J Phys Chem C 2024;128:516–24. https://doi.org/10.1021/acs.jpcc.3c06479.

[29] Kumar MP, Sadashivappa K, Prabhukumar GP, Basavarajappa S. Dry sliding wear behaviour of garnet particles reinforced zinc-aluminium alloy metal matrix composites. Mater Sci 2006;12(3):209–13.

[30] Singh RK, Maurya NK, Saxena A, Pandey A, Verma SK. Development and Characterization of Functionally Graded Al2024-Ni Metal Matrix Composite Leaf Plate under T3 Heat Treatment: RK Singh et al. MAPAN. 2025. p. 1–12.

[31] Singh RK, Singh RC. Investigation of microstructural, mechanical, and damping properties of B4C reinforced Al 7075 T6 Matrix. J Reinforc Plast Compos 2025: 07316844251337258.